Multiscale modeling of the effect of sub-ply voids on the failure of composite materials

Turteltaub, Sergio; de Jong, Gijs

Important note
To cite this publication, please use the final published version (if applicable).
Please check the document version above.

Multiscale modeling of the effect of sub-ply voids on the failure of composite materials

Sergio Turteltaub*, Gijs de Jong

Delft University of Technology, Faculty of Aerospace Engineering, Kluyverweg 1, 2629 HS Delft, the Netherlands

ARTICLE INFO

ABSTRACT

A multiscale fracture model is developed to study the influence of defects appearing at a microscale in a fiber-reinforced composite laminate. The model establishes a link between the geometrical characteristics of sub-ply imperfections that may be created during manufacturing and the overall fracture strength and fracture energy of the composite. In particular, a recently-developed multiscale theory is expanded to account for microvoids inside the matrix and gaps between closely-spaced fibers that prevent filling. These defects are explicitly incorporated in finite element simulations to study their influence on the on-set and propagation of cracks at the sub-ply level. To connect these microcracks to the effective fracture behavior at a ply-level, a computational homogenization technique is applied to extract the energetically-equivalent macroscopic fracture properties. Through a parametric analysis of configurations, the influence of the void content (porosity), void type and void shape on the effective fracture strength and the effective fracture energy of a composite are quantified. Results show that the porosity is the main parameter influencing fracture properties while the shape of the defects and their type (matrix or interfiber) only play a secondary role. Furthermore, the influence of voids on the fracture properties appears to be strongly dependent on the loading conditions. In particular, for the range of porosity analyzed (up to 8%), the influence of voids in mode I on the transverse fracture strength is not significant but the transverse fracture energy decreases approximately linearly down to about 50% of its original value. In contrast, in mode II, the transverse fracture strength is significantly affected with increasing porosity. Furthermore, the transverse fracture energy depends nonlinearly on the porosity and the reduction is relatively more pronounced than for mode I.

1. Introduction

Defects that appear during manufacturing of composite materials may affect their effective (macroscopic) mechanical properties, in particular their fracture properties such as fracture strength and fracture energy during quasi-static, fatigue and impact loading (Bowles and Frimpong, 1992; Jeong, 1997; Summerscales, 1998; Costa et al., 2001; Hamidi et al., 2004; Scott et al., 2014; Maragoni et al., 2017). These defects can range from relatively large dry spots spanning a ply thickness to matrix microvoids smaller than the diameter of the fibers. Experimentally quantifying the influence of defects on the effective mechanical properties is a challenging task since, by their own nature, it is difficult to generate defects in a controlled fashion (i.e., changing defects while keeping all other parameters fixed Costa et al. (2001)). Due to this large experimental variability, it is usually not possible to uniquely ascribe an

effect to specific features in defects. However, recently-developed multiscale numerical techniques can assist in providing insight into the influence of defects through computational simulations. These techniques have the advantage of being able to control the types of defects included in the simulations and, thus, being able to establish a direct link between specific types of defects and their influence on the observable (macroscopic) properties.

The multiscale approach couples the macro and micro responses using a homogenization technique, which relies on the behavior of the fine scale to determine the response of the larger scale. This concept also enables the development of a failure criterion based on the micromechanical behavior of the composite, both in terms of initiation and evolution, and has been extensively used for composite materials (see, e.g., Xia et al., 2001; Hettich et al., 2008; Canal et al., 2009; Arteiro et al., 2015). In the present work, attention is given to two distinct types of microscopic defects, namely (i) microvoids inside the matrix and (ii) interfiber voids, which are gaps between closely-spaced fibers that appear when the resin is unable to flow between the fibers. These types of defects have been studied numerically using

* Corresponding author.
 E-mail address: S.R.Turteltaub@tudelft.nl (S. Turteltaub).

https://doi.org/10.1016/j.ijsolstr.2019.01.031
0020-7683/© 2019 Elsevier Ltd. All rights reserved.

micromechanical models in Vajari et al. (2013, 2014); Vajari (2015); Maragoni et al. (2016) where it was found that the microscopic voids have a large influence on both the macroscopic strength and propagation of damage. The present study investigates a similar situation to provide further insight on the influence of the microscopic characteristics of voids on the fracture properties. In particular, two novel aspects are included here: Firstly, from the theoretical point of view, a recently-developed multiscale technique (Turteltaub et al., 2018) is expanded to account for sub-ply (microscopic) defects and a new averaging technique is proposed to satisfy the scale transition requirements (crack-based Hill-Mandel condition). Secondly, a systematic parametric analysis is carried out until complete failure of the (numerical) specimens and, through a post-processing technique, the detailed results are condensed into effective material properties for that microstructure. Through parametric analyses it is possible to establish a relation between geometrical parameters such as void volume fraction and void size

the advantage of being relatively simple to implement and provide sufficient flexibility for the simulations.

A typical microscopic volume element with a periodic crack is shown in Fig. 2. The volume element also shows voids, some of which may end up in the path of a crack (or may in fact be a location where a crack originates). The bold line indicates segments of a crack (including possible disconnected segments), all of which have a net contribution to the macroscopic fracture properties, particularly the effective fracture energy.

In order to determine the effective fracture properties of a composite, the microscopic volume element is loaded with a given average strain $\bar{\boldsymbol{\epsilon}}$ until complete failure of the specimen. Denote as $V = \cup_{k=1}^{n_{\mathrm{v}}} V^{(k)}$ the collection of all voids $V^{(k)}$, $k = 1, \ldots, n_{\mathrm{v}}$, inside the volume element Ω and denote as Γ the collection of all cracked segments at the end of a quasi-static process that leads to complete failure. Using the nomenclature indicated in Fig. 2, the periodic boundary-value problem that simulates the cracking process is, in the absence of body forces, formulated as

$$
\begin{cases}
\operatorname{div} \boldsymbol{\sigma}(\boldsymbol{x}, t) = \mathbf{0} & \boldsymbol{x} \text{ in } \Omega \setminus (\Gamma \cup V) \\
\boldsymbol{t}^{+}(\boldsymbol{x}^{+}, t) = -\boldsymbol{t}^{-}(\boldsymbol{x}^{-}, t) & \boldsymbol{x} \text{ on } \Gamma \\
\boldsymbol{t}(\boldsymbol{x}, t) = \boldsymbol{t}^{\mathrm{v}}(\boldsymbol{x}, t) & \boldsymbol{x} \text{ on } \partial V \\
\boldsymbol{u}(\boldsymbol{x} + l_1 \boldsymbol{e}_1, t) - \boldsymbol{u}(\boldsymbol{x}, t) = l_1 \bar{\boldsymbol{\epsilon}}(t) \boldsymbol{e}_1 \quad \boldsymbol{t}(\boldsymbol{x} + l_1 \boldsymbol{e}_1, t) = -\boldsymbol{t}(\boldsymbol{x}, t) & \boldsymbol{x} \text{ on } \partial \Omega_3 \setminus (\Gamma \cup \partial V) \\
\boldsymbol{u}(\boldsymbol{x} + l_2 \boldsymbol{e}_2, t) - \boldsymbol{u}(\boldsymbol{x}, t) = l_2 \bar{\boldsymbol{\epsilon}}(t) \boldsymbol{e}_2 \quad \boldsymbol{t}(\boldsymbol{x} + l_2 \boldsymbol{e}_2, t) = -\boldsymbol{t}(\boldsymbol{x}, t) & \boldsymbol{x} \text{ on } \partial \Omega_4 \setminus (\Gamma \cup \partial V) \\
\boldsymbol{u}^{\pm}(\boldsymbol{x}^{\pm} + l_1 \boldsymbol{e}_1, t) - \boldsymbol{u}^{\pm}(\boldsymbol{x}^{\pm}, t) = l_1 \bar{\boldsymbol{\epsilon}}(t) \boldsymbol{e}_1 \quad \boldsymbol{t}^{\pm}(\boldsymbol{x}^{\pm} + l_1 \boldsymbol{e}_1, t) = -\boldsymbol{t}^{\pm}(\boldsymbol{x}^{\pm}, t) & \boldsymbol{x} \text{ on } \partial \Omega_3 \cap (\Gamma \cup \partial V) \\
\boldsymbol{u}^{\pm}(\boldsymbol{x}^{\pm} + l_2 \boldsymbol{e}_2, t) - \boldsymbol{u}^{\pm}(\boldsymbol{x}^{\pm}, t) = l_2 \bar{\boldsymbol{\epsilon}}(t) \boldsymbol{e}_2 \quad \boldsymbol{t}^{\pm}(\boldsymbol{x}^{\pm} + l_2 \boldsymbol{e}_2, t) = -\boldsymbol{t}^{\pm}(\boldsymbol{x}^{\pm}, t) & \boldsymbol{x} \text{ on } \partial \Omega_4 \cap (\Gamma \cup \partial V)
\end{cases}
\tag{1}
$$

distribution and the fracture strength and fracture energy of the composite under distinct loading modes.

The work is organized into two parts: the first part in Section 2 refers to an extension of the model developed in (Turteltaub et al., 2018) to explicitly take voids into account. This includes an extension of the strain and stress power decompositions to identify void-related terms. A new version of a crack-based Hill-Mandel condition is subsequently developed and verified. The second part in Section 3 contains a series of parametric analyses designed to study the influence of distinct geometrical features of the voids. The main findings are summarized in Section 4.

2. Microscale formulation with voids

2.1. Preliminaries

A typical cross section of a ply in a fiber-reinforced composite consists of carbon or glass fibers embedded in an epoxy matrix as shown in Fig. 1. In a hierarchical multiscale formulation, a material point at a macroscale corresponds to the collective behavior of all microscale material points inside a volume element such as the periodic volume element highlighted in the figure. The volume element can be subjected to distinct loading conditions (such as nominal mode I, II or mixed mode) based on the chosen values of an average (macroscopic) strain tensor $\bar{\boldsymbol{\epsilon}}$ imposed on the element. For problems without fracture, periodic boundary conditions are generally preferred since they conform more closely to the actual material behavior and allow faster convergence in terms of the size of a representative volume element compared to linear displacement conditions or uniform traction. For problems involving fracture, periodic boundary conditions can also be applied since this allows modelling of a macroscopic crack without the need to specify a priori the crack orientation (see e.g., (Turteltaub et al., 2018) for details). Alternative boundary conditions may be used (see, e.g., (Coenen et al., 2012a; 2012b; Bosco et al., 2015; Svenning et al., 2016a; 2016b), but pointwise periodic boundary conditions have

where $\boldsymbol{\sigma}$ is the stress tensor, div is the divergence operator, $\boldsymbol{t}$ is the traction vector acting on the corresponding surface (Γ, $\partial \Omega$ or ∂V), $\boldsymbol{u}$ is the displacement vector and $\bar{\boldsymbol{\epsilon}} = \bar{\boldsymbol{\epsilon}}(t)$ corresponds to a prescribed macroscopic strain tensor applied on the volume element that drives the deformation process at different times t. The traction on the pores is given by a prescribed function $\boldsymbol{t}^{\mathrm{v}}$, which is typically zero unless the pores are filled with a fluid under pressure. The set $\Omega^{\mathrm{b}} := \Omega \setminus (\Gamma \cup V)$ refers to points in the bulk and the superscripts + and - refer to values on opposites sides of the surface Γ as illustrated in the figure.

The microscopic fracture process is solved numerically using intrinsic cohesive elements embedded within the bulk elements. This technique allows to model each material phase separately as well as the interfaces between the fibers and the matrix. The behavior of the matrix and the fibers can be specified with a constitutive model for the corresponding bulk elements, while the fracture behavior is modeled with traction-separation relations (i.e., cohesive relations see, e.g., Park and Paulino, 2011) which depend on the individual fracture strength and fracture energy of each phase or interface.

Care must be exercised during the post-processing of results to guarantee that the micro and macro scales quantities are energetically-consistent. In practice this means that one has to either guarantee a priori or to check a posteriori that the product of the effective macroscopic quantities (such as stress and strain rate) is equal to the volume average of the product of the corresponding microscopic quantities. This prerequisite in hierarchical multiscale modelling, known as the scale transition condition, the macrohomogeneity condition or, more commonly, as the Hill-Mandel condition, is an essential requirement that needs to be satisfied in an energetically-consistent multiscale formulation (see, e.g., Saeb et al., 2016 and the references therein). For problems involving fracture, the Hill-Mandel condition requires special treatment since damage localizes in interfaces (Gitman et al., 2007; Nguyen et al., 2010; Unger, 2013). In the present work, a crack-based Hill-Mandel condition developed in Turteltaub et al. (2018) is further extended to include the presence of voids. In many cases of practical interest the voids may be assumed to be traction-free from
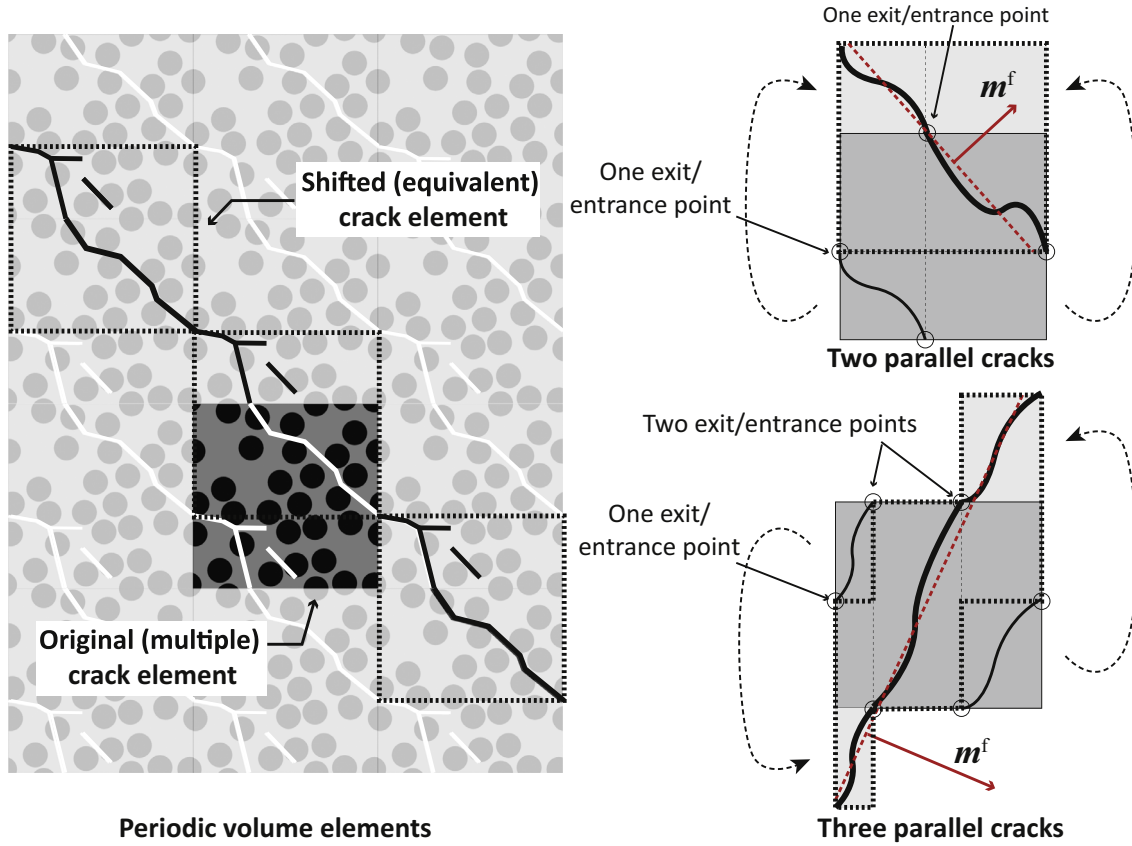
Fig. 1. Periodic volume element in a cross-section of a fiber-reinforced composite. The type of loading is specified through the chosen values $\bar{\boldsymbol{\epsilon}}$ of the average (macroscopic) strain tensor. As shown in Turteltaub et al. (2018), the corresponding localized crack repeats itself periodically but its effective orientation is not geometrically constrained by periodicity and can be interpreted as a single (isolated) crack while parallel periodic cracks may be ignored.
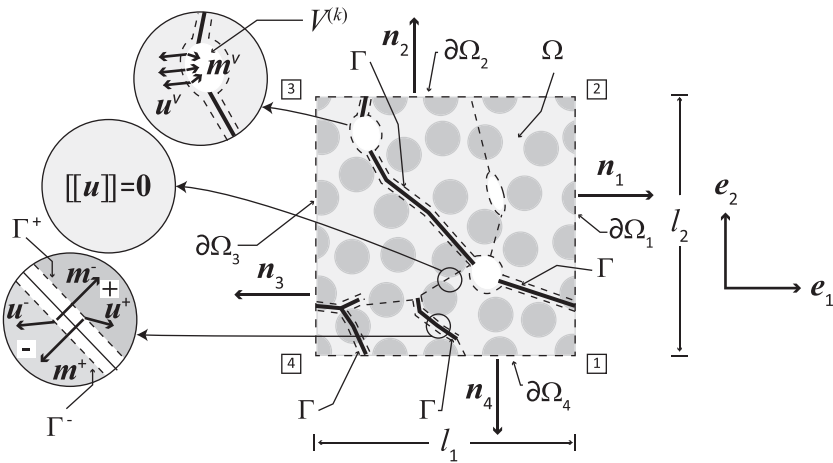

Fig. 2. Nomenclature used in a microstructural volume element Ω. The dashed lines indicate a partition of the domain used to compute integrals in subdomains.

the outset, so they do not directly contribute to the fracture energy (i.e., $\boldsymbol{t}^{\mathrm{v}} = \boldsymbol{0}$ in (1)). However, even in the traction-free case, the presence of voids needs to be taken into account when comparing quantities such as the average stress power per unit volume and the stress power rate from the product of the average stress and the average strain rate. To this end, the strain is decomposed into bulk, crack and void contributions in order to separate the effective quantities associated to the fracture process from those related to the bulk process.

2.2. Strain decomposition

The applied strain $\bar{\boldsymbol{\epsilon}}$ acting on a volume element Ω is by definition given as

$$\bar{\boldsymbol{\epsilon}} := \frac{1}{|\Omega|} \int_{\partial\Omega} [\boldsymbol{u} \otimes \boldsymbol{n}]_{\mathrm{sym}} \mathrm{d}s$$

with the notation $[\cdot]_{\mathrm{sym}}$ indicating the symmetric part of the tensor, $\boldsymbol{n}$ representing the outward normal unit vector as indicated in

Fig. 2, $\otimes$ corresponding to the tensor product and $|\Omega|$ the volume (area per unit depth) of the volume element Ω. In order to identify the part of the deformation in the volume element associated to the fracture process, consider a partition of Ω into subdomains as indicated by dashed lines in Fig. 2. The partition is such that the subdomains contain all cracked surfaces Γ and all void surfaces ∂V. To cover the whole domain using simply-connected subdomains, the partition can be complemented by divisions across uncraked bulk material where the displacement field is continuous. As indicated in Fig. 2, if the displacement field is continuous, the corresponding jump is zero, (i.e., $[\![\boldsymbol{u}]\!] = \boldsymbol{0}$, with $[\![(\cdot)]\!] = (\cdot)^+ - (\cdot)^-$ denoting the jump of a quantity $(\cdot)$ across a surface and with the superscripts + and - referring to the values of the quantity on opposites sides of the surface.) Making use of the divergence theorem in each subdomain separately and collecting all integrals it follows that the applied strain $\bar{\boldsymbol{\epsilon}}$ can be decomposed as follows:

$$\bar{\boldsymbol{\epsilon}} = \boldsymbol{\epsilon}^{\mathrm{b}} + \boldsymbol{\epsilon}^{\mathrm{f}} + \boldsymbol{\epsilon}^{\mathrm{v}} \tag{2}$$

where the bulk strain $\boldsymbol{\epsilon}^{\mathrm{b}}$, the fracture strain $\boldsymbol{\epsilon}^{\mathrm{f}}$ and the "void strain" $\boldsymbol{\epsilon}^{\mathrm{v}}$ are defined as

$$\boldsymbol{\epsilon}^{\mathrm{b}} := \frac{1}{|\Omega|} \int_{\Omega^{\mathrm{b}}} \boldsymbol{\epsilon} \mathrm{d}v \qquad \boldsymbol{\epsilon} = \frac{1}{2}\left(\nabla\boldsymbol{u} + (\nabla\boldsymbol{u})^{\mathsf{T}}\right)$$

$$\boldsymbol{\epsilon}^{\mathrm{f}} := \frac{1}{|\Omega|} \int_{\Gamma} [[\![\boldsymbol{u}]\!] \otimes \boldsymbol{m}]_{\mathrm{sym}} \mathrm{d}s$$

$$\boldsymbol{\epsilon}^{\mathrm{v}} := -\frac{1}{|\Omega|} \int_{\partial V} [\boldsymbol{u} \otimes \boldsymbol{m}]_{\mathrm{sym}} \mathrm{d}s \tag{3}$$

with the superscript T referring to the transpose. Observe that in the definition of the void strain there is a negative sign that reflects the sign convention indicated in the inset in Fig. 2 whereby the normal vector $\boldsymbol{m} = \boldsymbol{m}^{\mathrm{v}}$ on the void surface ∂V is defined in the outward direction from the bulk and hence inwards with respect to the void. In this way an *increase* in the volume of the void, for example with $\boldsymbol{u}$ and $\boldsymbol{m}$ oriented in the same normal direction but pointing in opposite senses, results in a *positive* normal void strain.

2.3. Stress power decomposition

The stress power P^{ext} (power per unit volume) applied on the external boundary of the volume element can be decomposed in terms of the stress power in the bulk, P^{b}, the rate of work on the crack surface, P^{f}, and a power term related to the voids, denoted as P^{v}. The main ingredient required for the stress power decomposition is the balance of linear momentum for a quasi-static process (without body force, as indicated in (1)), which is then multiplied by the velocity field $\dot{\boldsymbol{u}}$ and integrated by parts in the volume element. Similar to the strain decomposition, the stress power decomposition requires repeated use of the divergence theorem, for which one can partition the volume element Ω into subdomains as indicated in Fig. 2. As before, the divergence theorem is used separately in each sub-domain and the integrals are then added using the sign conventions indicated in Fig. 2, which yields

$$P^{\mathrm{ext}} = P^{\mathrm{b}} + P^{\mathrm{f}} - P^{\mathrm{v}} \tag{4}$$

where

$$P^{\mathrm{ext}} := \frac{1}{|\Omega|} \int_{\partial\Omega} \boldsymbol{t} \cdot \dot{\boldsymbol{u}} \mathrm{d}s$$

$$P^{\mathrm{b}} := \frac{1}{|\Omega|} \int_{\Omega^{\mathrm{b}}} \boldsymbol{\sigma} \cdot \dot{\boldsymbol{\epsilon}} \mathrm{d}v$$

$$P^{\mathrm{f}} := \frac{1}{|\Omega|} \int_{\Gamma} \boldsymbol{t} \cdot [\![\dot{\boldsymbol{u}}]\!] \mathrm{d}s$$

$$P^{\mathrm{v}} := \frac{1}{|\Omega|} \int_{\partial V} \boldsymbol{t}^{\mathrm{v}} \cdot \dot{\boldsymbol{u}} \mathrm{d}s. \tag{5}$$

It is in principle possible to formally view the boundaries of the pores, ∂V, as an "external" surface with a prescribed "external"

traction but, since it is more natural to view it as an internal surface with a known traction, the term P^{v} is accounted for on the right hand side of the decomposition (4). Correspondingly, the term "external" stress power, P^{ext}, is reserved for the rate of work done on $\partial\Omega$. Hence, if a pore intersects the boundary $\partial\Omega$, it may be still interpreted as an internal boundary. The term P^{b} accounts for the stress power in the uncracked material (bulk) that occupies the region Ω^{b} as indicated above. For the fracture process, the relevant term is the rate of work on the cracked surface, P^{f}, which does *not* include the pores. Finally, the term P^{v}, which accounts for the rate of work done by an imposed traction $\boldsymbol{t} = \boldsymbol{t}^{\mathrm{v}}$ acting on the surfaces of the pores, may be relevant for situations when the pores are filled with, for example, a pressurized fluid. In that case a separate model is required to determine the applied traction on the pores. However, for many structural applications of interest, it may be assumed that this term is negligible compared to other loads applied to the structure.

2.4. Identification of crack, solid and pores contributions

In the framework of hierarchical multiscale analysis, the effective (macroscopic) quantities are often defined from the outset as volume or surface averages of their microscopic counterparts. If the deformation does not localize inside a volume element (e.g., no localized plasticity or cracks appear), then the volume-based Hill-Mandel condition can be satisfied using, for example, periodic boundary conditions in order to guarantee a priori consistency across length scales. In that case the product of the averages is equal to the average of the products.

In the context of localized failure, however, the situation is more complex in the sense that the effective quantities in localized models may not expressed directly as a surface or volume average of their microscopic counterparts. Consequently, in that case the Hill-Mandel condition may not be satisfied a priori. A simple solution to this issue is to invert the role of the Hill-Mandel condition. Using this approach, the effective macroscopic quantities are in fact defined (or calibrated) from the Hill-Mandel condition. In that fashion, the traditional volume (or surface) average definition of a quantity is replaced by an energy-based definition that automatically guarantees consistency across scales. Periodic boundary conditions may still be used to satisfy the corresponding volume-based Hill-Mandel condition and definitions of effective quantities for fields associated to the bulk material in the neighborhood of a localized crack.

A crack-based Hill-Mandel condition, in a domain containing voids, can be established from the decomposition of the strain and the stress power as developed in Sections 2.2 and 2.3. The guiding principle in the foregoing analysis is the need to establish a relation between the rate of work associated to the fracture process, i.e., P^{f} as defined in (5), and the product between an effective cohesive traction $\boldsymbol{t}^{\mathrm{f}}$ and an effective crack opening rate $[\![\dot{\boldsymbol{u}}]\!]^{\mathrm{f}}$ for a homogenized traction-separation relation that may be used at a macroscale. Simultaneously, a separate requirement is to preserve the volume-based definitions of effective fields commonly used in multiscale analysis in the absence of localization, particularly for the rate of work P^{b} as indicated in (5).

It is convenient to introduce the following notation for bulk-averaged and crack-averaged quantities:

$$\langle(\cdot)\rangle_{\Omega} := \frac{1}{|\Omega|} \int_{\Omega^{\mathrm{b}}} (\cdot) \mathrm{d}v \quad \langle(\cdot)\rangle_{\Gamma} := \frac{1}{|\Gamma|} \int_{\Gamma} (\cdot) \mathrm{d}s.$$

Using periodic boundary conditions, it can be shown that the external stress power P^{ext} defined in (5) satisfies the following relation:

$$P^{\mathrm{ext}} = \langle\boldsymbol{\sigma}\rangle_{\Omega} \cdot \dot{\bar{\boldsymbol{\epsilon}}}$$

that corresponds to the classical (volume-based) Hill-Mandel macrohomogeneity condition. Consequently, the effective (macroscopic) stress tensor corresponds to the volume average of its microscopic counterpart. However, upon the formation of a localized crack, the traction vector on planes other than the crack itself may become discontinuous, hence the stress tensor is discontinuous. The traction across the crack surface during the cracking process remains continuous. The purpose of the foregoing analysis is to establish a relation for the traction on the cracked surface during decohesion. Using the decompositions (2) (in time-rate form) and (4) in the relation above yields

$$P^b + P^f - P^v = \langle\boldsymbol{\sigma}\rangle_\Omega \cdot \langle\dot{\boldsymbol{\epsilon}}\rangle_\Omega + \langle\boldsymbol{\sigma}\rangle_\Omega \cdot \dot{\boldsymbol{\epsilon}}^f + \langle\boldsymbol{\sigma}\rangle_\Omega \cdot \dot{\boldsymbol{\epsilon}}^v.$$

Consequently, from the strain and power decompositions, it is natural to identify three separate relations associated to scale transitions as follows:

Rate of work in/on	Microscale term	Proposed macroscale equivalent
Bulk	P^b	$\langle\boldsymbol{\sigma}\rangle_\Omega \cdot \langle\dot{\boldsymbol{\epsilon}}\rangle_\Omega$
Crack surfaces	P^f	$\langle\boldsymbol{\sigma}\rangle_\Omega \cdot \dot{\boldsymbol{\epsilon}}^f$
Void/pore surfaces	P^v	$-\langle\boldsymbol{\sigma}\rangle_\Omega \cdot \dot{\boldsymbol{\epsilon}}^v$

(6)

Observe that the negative sign in the expression for the voids is a consequence of the sign convention whereby the normal vector points outwards from the solid and into the void. It should be emphasized that the aforementioned identifications are assumptions that need to be verified a posteriori.

2.5. A crack-based Hill-Mandel condition

From a modelling point of view, pores may be handled in two possible ways: (i) treat the pores as entities separate from the bulk and the crack or (ii) combine pores with the effective behavior of the bulk and/or the crack. For example, pores that are in the path of a crack may be combined with the crack itself while isolated pores may be combined with the bulk material. However, if the traction prescribed on the pore surfaces is not zero, combining the pores with the crack may cause modelling problems in the form of a residual cohesive traction that is connected to the loading and does not represent the actual fracture behavior of the material. To resolve this issue, a more robust approach is to combine *all* the pores with the bulk behavior regardless of their location (i.e., whether they are on the crack path or not). Pores induce stress concentrations and further facilitate cracking, which generally affects the fracture strength and energy. Hence, although the pores are formally not considered as part of the crack, their presence has a strong influence on the effective traction-separation relations. In line with this consideration, unless explicitly indicated, the "bulk" refers henceforth to the combined solid and porous parts while the "crack" refers to the surfaces created during the cracking process but excluding pre-exisiting pores. Consequently, the crack-based Hill-Mandel condition is treated separately from the combined solid and porous parts.

As discussed in Nguyen et al. (2010) and Turteltaub et al. (2018), to prevent RVE convergence problems related to non-constant surface-to-volume ratios for volume elements of distinct size, it is important to average fracture properties on the crack surface instead than on the volume element. To this end, multiply the crack-based stress power P^f in (3) and the corresponding term $\langle\boldsymbol{\sigma}\rangle_\Omega \cdot \dot{\boldsymbol{\epsilon}}^f$ (as shown in (6)) by the factor $|\Omega|/|\Gamma|$ to get, in view of (5), the following correspondence relation:

$$\langle\boldsymbol{t} \cdot [[\dot{\boldsymbol{u}}]]\rangle_\Gamma \leftrightarrow \langle\boldsymbol{\sigma}\rangle_\Omega \cdot \langle[[[\boldsymbol{u}]] \otimes \boldsymbol{m}]_{\text{sym}}\rangle_\Gamma. \tag{7}$$

The symbol $\leftrightarrow$ is used in (7) to emphasize that equality is not a priori guaranteed but, rather, it is a proposed scale transition requirement.

2.6. Effective fracture behavior

For a cohesive-zone modelling approach at the macroscopic level, the model should involve two ingredients: (i) a nucleation criterion (i.e., under what loading conditions and in which orientation a crack is first detected at the macroscopic length scale) and (ii) an evolution model (i.e., how does the cohesive traction evolves with crack opening). Although an inelastic process should normally be expressed in rate form to account for path-dependency, it is customary in the cohesive zone framework to model the cracking process using directly a relation between an (effective) cohesive traction $\boldsymbol{t}^f$ and an effective crack opening $[[\boldsymbol{u}]]^f$. In addition, due to the scale transition, the macroscopic description requires an effective crack length $|\Gamma^f|$ associated with a macroscopic crack within a volume element as illustrated in Fig. 3.

An important issue is the definition of the effective quantities $|\Gamma^f|$, $\boldsymbol{t}^f$ and $[[\boldsymbol{u}]]^f$. Observe that, in combination with (3), the right hand side of relation (7), which should refer to the effective properties, involves tensorial quantities (i.e., $\langle\boldsymbol{\sigma}\rangle_\Omega$ and $\boldsymbol{\epsilon}^f$) and not vectors (i.e., $\boldsymbol{t}^f$ and $[[\boldsymbol{u}]]^f$) as commonly-used in a traction-separation relation. The relation between these quantities is not trivial since it involves itself a scale transition (e.g., $\langle\boldsymbol{t}\rangle = \langle\boldsymbol{\sigma}\boldsymbol{n}\rangle$ is generally different than $\langle\boldsymbol{\sigma}\rangle\langle\boldsymbol{n}\rangle$ and a similar observation applies for the fracture strain tensor and crack opening vector).

From a geometrical point of view it is natural to define the effective crack opening rate as the surface average of its microscopic counterpart, scaled with the ratio of effective to actual crack length, i.e.,

$$[[\boldsymbol{u}]]^f := \frac{|\Gamma|}{|\Gamma^f|}\langle[[\boldsymbol{u}]]\rangle_\Gamma \tag{8}$$

where the effective crack length $|\Gamma^f|$ is obtained from the geometry of a volume element using the approach proposed in Turteltaub et al. (2018), i.e.,

$$|\Gamma^f| := \begin{cases} |\Gamma^f_{\min}| & \text{if } r \geq r_{\max} \\ |\Gamma^f_{\max}| & \text{if } r < r_{\max} \end{cases} \tag{9}$$
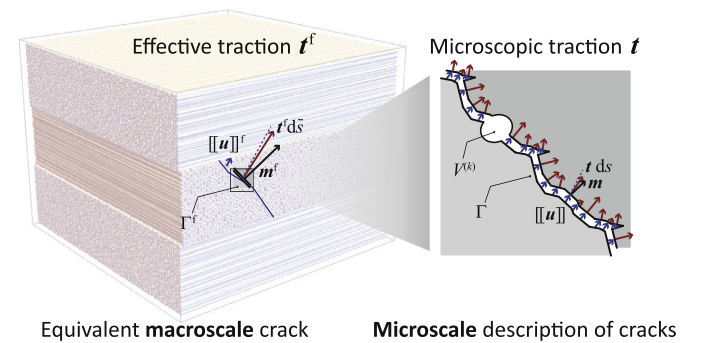

Fig. 3. Illustration of a sub-ply volume element with a microscopic crack (right) and equivalent macroscale crack (left) with effective normal vector $\boldsymbol{m}^f$, effective cohesive traction $\boldsymbol{t}^f$ and effective crack opening $[[\boldsymbol{u}]]^f$. Observe that here the notion of macroscale refers to a larger scale compared to the microscale but still within a single ply in a laminate.

where, using the notation shown in Fig. 2,

$$\left|\Gamma^{\mathrm{f}}_{\min}\right| := \min\left(\frac{l_1}{|\boldsymbol{n}_2 \cdot \boldsymbol{m}^{\mathrm{f}}|}, \frac{l_2}{|\boldsymbol{n}_1 \cdot \boldsymbol{m}^{\mathrm{f}}|}\right)$$

$$\left|\Gamma^{\mathrm{f}}_{\max}\right| := \max\left(\frac{l_1}{|\boldsymbol{n}_2 \cdot \boldsymbol{m}^{\mathrm{f}}|}, \frac{l_2}{|\boldsymbol{n}_1 \cdot \boldsymbol{m}^{\mathrm{f}}|}\right) \qquad r := \frac{\left|\Gamma^{\mathrm{f}}_{\max}\right|}{\left|\Gamma^{\mathrm{f}}_{\min}\right|} \qquad (10)$$

and with the effective crack normal being defined as

$$\boldsymbol{m}^{\mathrm{f}} := \langle \boldsymbol{m} \rangle_{\Gamma}. \qquad (11)$$

The previous expression is based on the notion that the effective crack length $|\Gamma^{\mathrm{f}}|$ should correspond to the length of a straight segment crossing periodically the volume element in a direction perpendicular to $\boldsymbol{m}^{\mathrm{f}}$. The value r represents the number of crossings of a straight periodic crack along a periodic $l_1 \times l_2$ rectangular domain (either bottom to top or left to right). In general, however, it is not possible to construct a straight periodic crack with the given vector $\boldsymbol{m}^{\mathrm{f}}$ (i.e., r is not an integer unless the orientation of $\boldsymbol{m}^{\mathrm{f}}$ satisfies a specific geometrical relation with l_1 and l_2). Consequently, $|\Gamma^{\mathrm{f}}|$ is interpreted as an approximation. Further, the cut-off value $r_{\max}$ is introduced to handle near vertical (or near horizontal) periodic cracks. In practice a maximum value of $r_{\max} = 5$ has proven to be sufficient to distinguish between vertical (or horizontal) and near vertical (or near horizontal) cracks. It is observed that, since the microscale crack may contain multiple branches (bifurcations) and/or isolated segments, care must be exercised to preserve consistency in the sign conventions of Γ^+ and Γ^- when performing the integration on Γ. Further, this also implies that the ratio $|\Gamma|/|\Gamma^{\mathrm{f}}|$ may deviate from unity, with values smaller than 1 also being possible for cracks that contain voids in their paths.

As indicated above, it is convenient to tie the definition of the effective cohesive traction to the relation (7), i.e., $\boldsymbol{t}^{\mathrm{f}}$ can be implicitly defined such that

$$\left|\Gamma^{\mathrm{f}}\right|\boldsymbol{t}^{\mathrm{f}} \cdot [\![\boldsymbol{u}]\!]^{\mathrm{f}} := |\Gamma|\langle\boldsymbol{\sigma}\rangle_{\Omega} \cdot \left\langle [[\![\boldsymbol{u}]\!] \otimes \boldsymbol{m}]_{\mathrm{sym}} \right\rangle_{\Gamma}. \qquad (12)$$

Correspondingly, in view of (7), (8) and (12), $\boldsymbol{t}^{\mathrm{f}}$ is defined such that the macroscopic description of the rate of work coincides with the microscopic one. One limitation with the previous definition is that the part of the traction that is perpendicular to the crack opening rate remains undetermined (i.e., the formula would only specify the projection of $\boldsymbol{t}^{\mathrm{f}}$ into $[\![\boldsymbol{u}]\!]^{\mathrm{f}}$). Furthermore, from an implementation point of view, the calculation of $\boldsymbol{t}^{\mathrm{f}}$ from (12) may be prone to errors due to inaccuracies in the computation of the instantaneous values of the local crack opening rates. As indicated in Turteltaub et al. (2018), an alternative approach is to propose a general form for $\boldsymbol{t}^{\mathrm{f}}$ with a calibration parameter that is then adjusted to satisfy relation (12). Adopting that approach, the proposed approximation for the effective cohesive traction is as follows:

$$\boldsymbol{t}^{\mathrm{f}} \approx \alpha \boldsymbol{t}^{\mathrm{f}}_{\Gamma} + (1 - \alpha)\boldsymbol{t}^{\mathrm{f}}_{\Omega} \qquad (13)$$

where α is a calibration parameter and the crack-based cohesive traction $\boldsymbol{t}^{\mathrm{f}}_{\Gamma}$ and volume-based cohesive traction $\boldsymbol{t}^{\mathrm{f}}_{\Omega}$ are defined as

$$\boldsymbol{t}^{\mathrm{f}}_{\Gamma} := \langle \boldsymbol{t} \rangle_{\Gamma} \qquad \boldsymbol{t}^{\mathrm{f}}_{\Omega} := \langle \boldsymbol{\sigma} \rangle_{\Omega}\boldsymbol{m}^{\mathrm{f}}. \qquad (14)$$

The (phenomenological) parameter α is taken here as a time-independent quantity that is meant to approximately enforce (12) in a time-averaged fashion (i.e., throughout the entire cracking process), thus it should not be used to enforce the scale transition relation at each time separately, which would require a variable parameter. To emphasize the rationale of this approach, in the present work (12) is viewed as a definition of the effective traction whereas (13) is taken as an approximation used to enforce the definition. In view of (8), (11), (12), (13), and (14), the parameter α

can be obtained through the post-processing of simulation data of a fracture process from $t = 0$ (initial state) to $t = T$ (fully-damaged state), from the following relation:

$$\alpha = \frac{\int_0^T (\langle\boldsymbol{t}\rangle_{\Gamma} - \langle\boldsymbol{\sigma}\rangle_{\Omega}\langle\boldsymbol{m}\rangle_{\Gamma}) \cdot \langle [\![\dot{\boldsymbol{u}}]\!]\rangle_{\Gamma}\mathrm{d}t}{\int_0^T \langle\boldsymbol{\sigma}\rangle_{\Omega} \cdot (\langle [\![\dot{\boldsymbol{u}}]\!] \otimes \boldsymbol{m}\rangle_{\Gamma} - \langle [\![\dot{\boldsymbol{u}}]\!]\rangle_{\Gamma} \otimes \langle\boldsymbol{m}\rangle_{\Gamma})\mathrm{d}t}.$$

After establishing consistency in energy between micro and macroscales, the next step is to determine the actual effective properties (i.e., converged quantities with respect to sample size). To this end, microscopic volume elements of increasing size are subjected to the same nominal load to determine (numerically) the minimum size of the representative volume element (RVE), which corresponds to the smallest one for which the fracture properties are no longer dependent upon the size of the volume element to within a prescribed tolerance (see e.g. Kanit et al. (2003)). In the context of localization, one may refer to the equivalent crack as a representative *surface* element (RSE) embedded in an RVE. This analysis requires multiple samples of volume elements of the same size to compute the mean of all realizations, although in practice it may be required to use a relatively large convergence tolerance and/or to limit the number of samples due to the overall computational cost. This is because in each convergence analysis for the volume element size, the numerical results must also converge, thus a separate mesh refinement convergence test must be carried out for each volume element. This convergence test is particularly important in the context of fracture since there is a process of localization (i.e., the formation of a crack) which requires a non-traditional convergence analysis (see e.g. Turteltaub et al., 2018 for details). Once the minimum acceptable size of the RVE has been established, parametric analyses can be conducted to study the influence of physical and geometrical parameters associated to defects as explained in the next section.

3. Simulations with volume elements containing voids

3.1. Overview of simulation cases

In order to study the effect of sub-ply porosities, several cases are analyzed using distinct types of samples as illustrated in Fig. 4. For simplicity, a plane strain framework is adopted assuming that in the out-of-plane direction (longitudinal direction of the fibers) the dimensions of the sample are large compared to the size of the computational domain (cross-section in the interior of a sample). Porosities of 0%, 1%, 2%, 4%, 6% and 8% were considered (measured per unit cross-sectional area). For each porosity, two distinct types of voids are analyzed, namely matrix voids and interfiber voids. In addition, for the matrix voids, two types of cases are considered separately, namely one where all voids have the same characteristic size and one with variable size and aspect ratio using randomly-oriented ellipses. The setup consisting of matrix voids of constant size is seen as a baseline for a given porosity (with the case of no porosity being the overall benchmark to study the effect of porosity). Cases with interfiber voids (with interfiber voids up making up about 1/4 of the voids and the rest being matrix voids), are used to gage the effect of the type of microscopic void. Other effects are studied by varying the size of the individual pores and their aspect ratio while keeping the porosity fixed, as indicated above.

Since the effect of defects is expected to depend on the loading conditions, two representative loading cases were considered for each configuration as indicated in Table 1. The two cases, expressed in terms of the applied macroscopic strain tensor $\bar{\boldsymbol{\epsilon}}$, with $\gamma > 0$ acting as a strain parameter, induce cracking in a cross-section perpendicular to the fiber direction (i.e., lateral cracking).

To account for statistical variations in the microstructure, eight random realizations are considered for each porosity, for each void
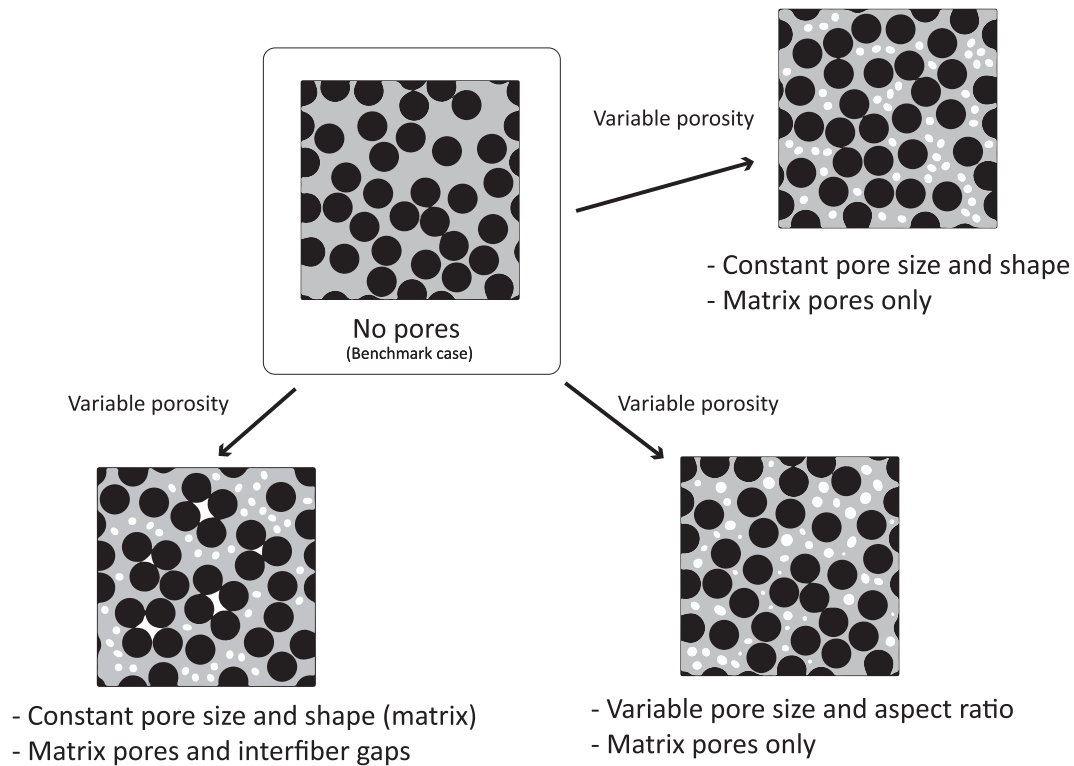
Fig. 4. Illustration of parametric study for defects: for porosities from 0 to 8% distinct configurations are analyzed in terms of void type, shape and size.

Table 1

Load cases expressed in terms of the applied macroscopic in-plane strain tensor $\bar{\boldsymbol{\epsilon}}$, with $\gamma > 0$ a strain parameter. Observe that the pure shear is applied at an angle of 45° with respect to the coordinate system shown in Fig. 2.

Load cases	Applied in-plane strain
1. Laterally-constrained uniaxial extension	$\begin{bmatrix} \bar{\epsilon}_{11} & \bar{\epsilon}_{12} \\ \bar{\epsilon}_{21} & \bar{\epsilon}_{22} \end{bmatrix} = \begin{bmatrix} \gamma & 0 \\ 0 & 0 \end{bmatrix}$
2. Pure Shear	$\begin{bmatrix} \bar{\epsilon}_{11} & \bar{\epsilon}_{12} \\ \bar{\epsilon}_{21} & \bar{\epsilon}_{22} \end{bmatrix} = \begin{bmatrix} \gamma & 0 \\ 0 & -\gamma \end{bmatrix}$

type and shape and for each load case. To achieve the target porosity in a sample, a discrete number of pores were used ranging from typically 6 pores for 1% porosity to about 50 pores at 8% porosity, with an average characteristic size of about 1.7 µm. In general more realizations are required to establish accurate statistical data, however the number is limited due to the overall computational cost. To further control the overall computational cost and in view of the large number of cases considered above, the material properties were kept fixed in all simulations and all samples had a fixed fiber volume fraction of (approximately) 50%, with the rest (matrix and voids) adding up to the remaining 50%. The material properties shown in Table 2 are representative of composite materials

typically encountered in the aerospace industry, and it is expected that the findings regarding the effect of microvoids would be similar for other composites with comparable properties.

Due to the large number of simulations, a dedicated python script was developed to generate the samples, generate the meshes, create the input files for the finite element analyses, run the simulations in parallel, execute the post-processing and generate the results. The simulations were carried out using the Finite Element package Abaqus (2018) using linear plane strain elements for the bulk (matrix and fiber) and cohesive elements with linear softening to capture the fracture process. Unstructured meshes were produced using the mesh generator Gmsh (2018) with the goal to minimize the mesh dependency of the crack pattern. The cohesive elements were embedded between all edges of the bulk elements (including fibers). Mesh refinement analysis was systematically carried out for all samples of all sizes until a converged mesh was identified within a given tolerance. The convergence analysis to identify the size of the representative volume element (or, more specifically, the representative surface element for an equivalent crack) was done with the corresponding converged mesh for each sample size. It was established that for a volume element of 75 µm × 75 µm the mean response was within the tolerance of a (discrete) deviation of the previous size volume ele-

Table 2

Material properties of a typical composite system used in aerospace applications. Elastic properties are taken from HexTow IM7 fibers and CYCOM 5230-2 matrix. Fracture properties are not measured but are assumed to be representative (observe that the fiber-matrix interface is the weakest). Unless otherwise indicated and where applicable, the elastic and fracture properties for the matrix and the fiber are associated to (transversely-)isotropic models.

Property	Units	Fiber	Matrix	Fiber-matrix interface
Modulus of elasticity	GPa	19 (Transverse)	3.52	-
Poisson's ratio	-	0.23 (Transverse)	0.35	-
Fracture strength	MPa	100	50	25
Fracture energy	kJ/m² (=N/mm)	0.1	0.05	0.025

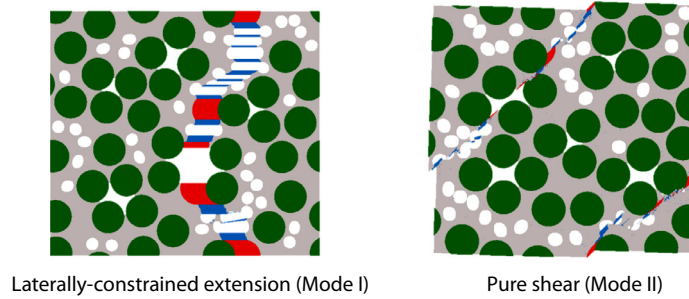Laterally-constrained extension (Mode I)   Pure shear (Mode II)

Fig. 5. Typical simulations for the case of 8% porosity under loading case 1 (laterally-constrained uniaxial extension shown on the left) and loading case 2 (pure shear shown on the right). Blue segments indicate crack opening in the matrix, red in the fiber-matrix interface and the rest in the matrix voids and interfiber voids. The effective cracks for loading cases 1 and 2 appeared (on average) as opening modes I and II, i.e., as normal and tangential openings, respectively. (For interpretation of the references to color in this figure legend, the reader is referred to the web version of this article.)

ment size 62.5 μm × 62.5 μm with a nominal mesh size parameter of 1 μm, although a locally refined mesh was used to capture the details of the voids. Typical simulations for loading cases 1 and 2 are shown in Fig. 5 for one realization of 8% porosity with matrix voids and interfiber voids.

In most cases the crack path contains portions through the matrix (shown as blue segments in color version), through the relatively weak matrix-fiber interface (shown as red segments) and through matrix and interfiber voids.

Due to its higher fracture strength and energy, no cracks were observed in the fibers. Further, since the fibers did not completely restrict the path of the cracks, an effective crack opening mode type I (normal) was observed in the simulations for loading case 1 while an effective crack opening mode type II (tangential) was triggered in the simulations for loading case 2. Correspondingly, the loading cases 1 and may be nominally interpreted as fracture modes I and II, respectively, when referred to a cross section perpendicular to the fiber direction. In general, the mode I simulations typically required the least computational effort, whereas mode II required small time steps to converge and hence a larger computational time. For conciseness, results of the convergence analysis are omitted here but some details can be found in de Jong (2018).

3.2. Matrix voids of constant size

The first set of simulations is carried out for matrix voids of constant size, which will be used subsequently as a benchmark

for a fixed porosity. The effective traction-separation relations for porosities ranging from 0% to 8% are shown in Fig. 6a under constrained uniaxial extension (nominal mode I) in terms of the normal component t_n^f of the cohesive traction vector t^f as a function of the normal component $[[u_n]]^f$ of the effective crack opening vector $[[u]]^f$. Similarly, the effective traction-separation relations under pure shear (nominal mode II) are shown in Fig. 6b in terms of the tangential cohesive traction component t_s^f as a function of the tangential effective crack opening component $[[u_s]]^f$. The lines plotted in the figures represent the average of eight realizations for each porosity, while the shaded regions in the graphics correspond to the (discrete) standard deviation. For clarity the standard deviation is only shown only for the porosity of 8%. For loading case 1 (nominal mode I), the tangential component was relatively small compared to the normal one and, conversely, for loading case 2 (nominal mode II), the normal component was relatively small compared to the tangential component.

Microscale failure, measured by monitoring individual cohesive elements, initiated in places intrinsically weak and prone to stress concentrations for both loading cases. However, microscale damage does not immediately translate into macroscopic failure. Indeed, as it is common in multiscale analysis of fracture, the onset of fracture at the microscale typically occurs during the early stages of the loading but can only be detected at the macroscale once sufficient damage has accumulated (see, e.g., Suiker and Turteltaub, 2007a; Suiker and Turteltaub, 2007b; Farle et al., 2018; Hille et al., 2011 for examples in distinct material systems). In the current
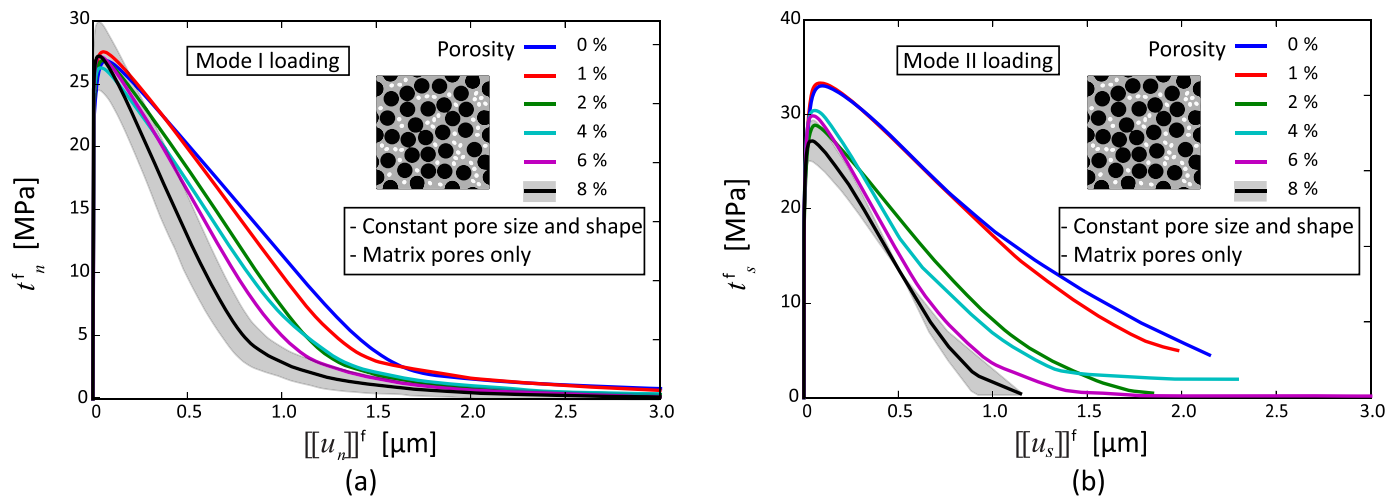

Fig. 6. Effective traction-separation relation for porosities varying from 0 to 8% for the case of matrix pores of constant size for (a) constrained uniaxial extension (nominal mode I) and (b) pure shear (nominal mode II). See text for further details.
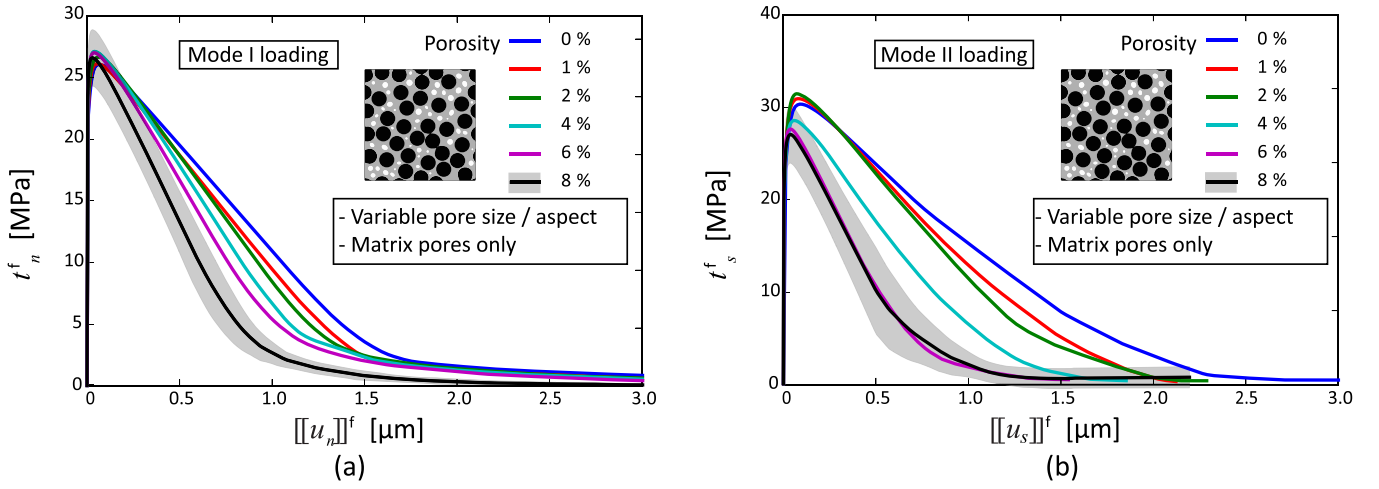
Fig. 7. Effective traction-separation relation for porosities varying from 0 to 8% for the case of matrix pores of variable size for (a) constrained uniaxial extension (mode I) and (b) pure shear (nominal mode II). See text for further details.

context, the first detectable onset of fracture at the macroscale is, by definition, measured by the peak value in the traction-separation relation, which is the (transverse) macroscale fracture strength of the ply under the corresponding loading case.

Once the representative volume element is completely damaged it can no longer transmit loads, in which case the energy dissipated due to fracture in the representative surface element corresponds to the macroscopic fracture energy. As may be observed from Fig. 6a, the fracture strength for mode I remains relatively constant for distinct porosities while the fracture energy (visually corresponding to the area under the traction-separation curve), decreases for increasing porosity. For mode II, as may be seen in Fig. 6b, both the fracture strength and the fracture energy decrease as a function of porosity. Observe that in Fig. 6b some curves do not terminate at zero traction; this is due to the fact that some of the realizations had convergence issues in shear when the crack was almost fully-formed. The curves in Fig. 6b, which are obtained as an average of multiple realizations, only reflect the portion for which all realizations converged. For the purpose of computing the effective fracture energy, which requires a response until complete damage, an interpolation to zero traction was used for the non-converged curves and averaged with the converged curves of the same porosity. The effective properties obtained through postprocessing of the simulations, particularly the fracture strength, are also strongly influenced by the fiber-matrix interface properties since this is the weakest component in the system (see Table 2). A quantitative analysis of the dependency on porosity is presented below in combination with the results from two other sets of simulations, namely matrix voids of variable size and voids of distinct types.

3.3. Matrix voids of variable size and aspect ratio

The second set of simulations is carried out for matrix voids of variable size and aspect ratio. The aspect ratios varied from 1 to 1.4 and the characterisitc sizes were derived from a normal distribution around the average characterisitic size. Due to the limited numbers of pores, however, only a few representative sizes were considered in each simulations ranging from 0.17 to 1.83 times the average characteristic size. As in the previous benchmark case of constant size, results are shown in this section for the two loading cases and various porosities in Fig. 7, ranging from 0% to 8%. In particular, Fig. 7a corresponds to the normal component t_n^f of the cohesive traction vector $\boldsymbol{t}^f$ as a function of the normal

component $[[u_n]]^f$ of the effective crack opening vector $[[\boldsymbol{u}]]^f$ under constrained uniaxial extension (nominal mode I), while Fig. 7b shows the effective tangential cohesive traction component t_s^f as a function of the tangential effective crack opening component $[[u_s]]^f$ under pure shear (nominal mode II). As before, the lines indicate the average response, over eight random realizations for each porosity, while the shaded areas illustrate the standard deviation (shown only for the porosity of 8%).

Similar qualitative observations can be drawn in this case compared to the previous set of simulations, namely a weak dependency of the fracture strength on porosity under constrained uniaxial extension, a decrease of the effective strength under pure shear with increasing porosity and, for both loading cases, a decrease in fracture energy with increasing porosity.

3.4. Matrix and interfiber voids

The third set of simulations is carried out for interfiber voids together with matrix voids of fixed size. As before, results are shown in Fig. 8 for the two loading cases and various porosities (0% to 8%). For constrained uniaxial extension the normal component t_n^f of the cohesive traction is shown in Fig. 8a as a function of the normal component of the effective crack opening, $[[u_n]]^f$, whereas for pure shear the tangential cohesive traction component t_s^f is shown as a function of the tangential effective crack opening component $[[u_s]]^f$ in Fig. 8b. Similar to the previous sets of simulations, the solid lines are obtained from the average of eight realizations while the shaded regions indicate the discrete standard deviation. In this case it is worth noting that, due to computational and geometrical limitations, only a limited amount of voids correspond to interfiber voids since these regions are formed by groups of three or four fibers that are in close proximity (see, e.g., Fig. 9). Although the net average distance between fibers is not greatly affected (i.e., negligible fiber clustering), these factors need to be taken into account in order to gage the net effect of interfiber voids. A comparative analysis of the simulation results of Figs. 6–8 is presented in the next section.

3.5. Comparative analysis

In order to quantify the influence of the geometrical features of the microstructure on the effective fracture properties, it is convenient to summarize all the results for each loading case separately.
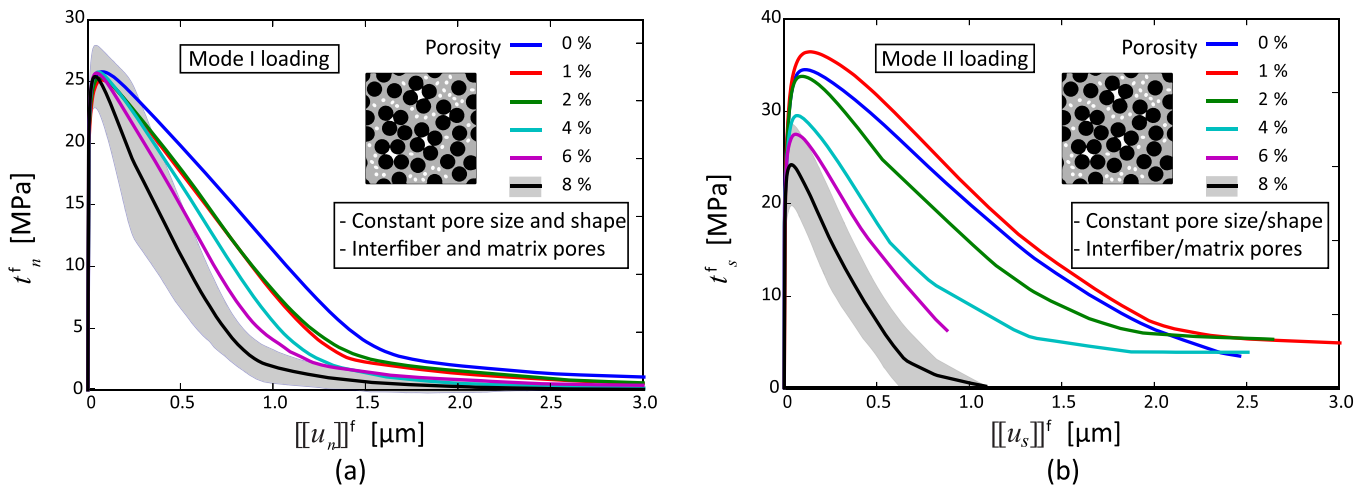
Fig. 8. Effective traction-separation relation for porosities varying from 0 to 8% for the case of interfiber voids and matrix pores of fixed size for (a) constrained uniaxial extension (mode I) and (b) pure shear (nominal mode II). See text for further details.
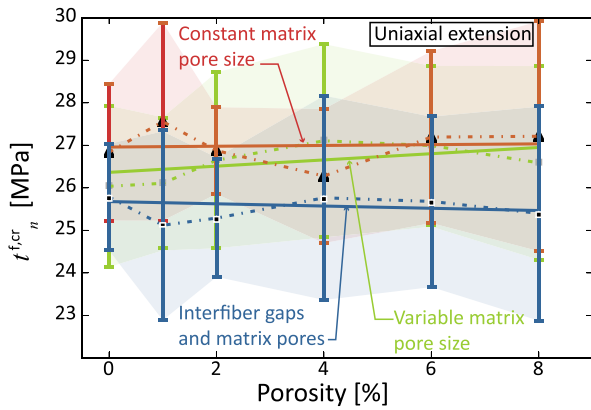

Fig. 9. Normal component of the effective fracture strength under uniaxial extension (mode I) as a function of porosity for different types and distributions of defects. The tangential component of the effective strength is negligible.
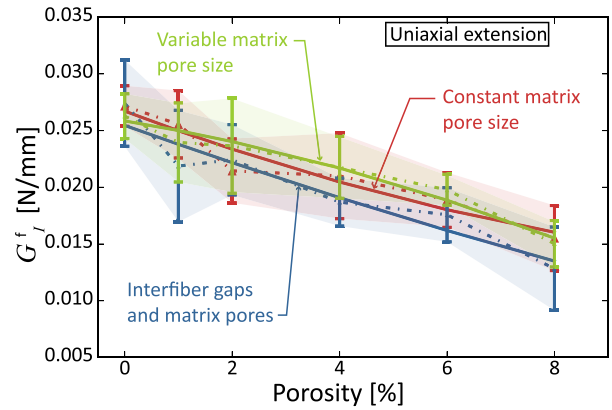
Fig. 10. Effective fracture energy G_I^f under uniaxial extension (mode I) as a function of porosity for different types and distributions of defects.

3.5.1. Comparative analysis for constrained uniaxial extension (mode I)

The normal component $t_n^{f,cr}$ of the effective (macroscopic) fracture strength under uniaxial extension is shown in Fig. 9 as a function of porosity for the three sets of voids analyzed (matrix voids of constant size, matrix voids of variable size and a mixture of interfiber voids and matrix voids). In all simulations, the cracks in the numerical samples open in a nominal mode I. The error bars at each porosity analyzed indicate the discrete standard deviation from the mean. To visualize the dependency of the fracture strength on porosity, the shaded regions indicate the upper and lower values of the standard deviation while the means for each set are connected with dashed lines. In addition, a linear fit for the means is shown as a solid line.

From Fig. 9, it may be observed that the effective fracture strength is dominated by the weakest component in the system, namely the fiber-matrix interfaces, with an effective value slightly above 25 MPa (see Table 2). This value, interestingly, remains relatively constant as a function of porosity. Although the interfiber voids case has a slightly lower effective strength, the differences are not significant compared to the matrix voids (with either constant or variable void size). It is relevant to recall that the amount of voids directly connected to interfiber voids is about 1/4 of the porosity, while the rest is composed of matrix voids, hence the effect due to interfiber voids is coupled to the effect of matrix voids.

A direct comparison of pure interfibers voids versus pure matrix voids was not carried out due to the limited range of porosity achievable with pure interfiber voids (up to 2%). For the 0% case (no voids), all three cases should in principle start from a common point. However, the deviations shown in the results at zero porosity between the three types of voids analyzed can be ascribed to the fact that these were obtained from distinct sets of realizations, hence the distinct values reflect the influence of the fiber distributions and not of the voids. In general, the simulation results indicate that, contrary to expectations, the fracture strength in mode I is relatively insensitive to defects up to the range of values analyzed.

The effective fracture energy G_I^f for the nominal mode I is shown in Fig. 10 as a function of porosity for the three sets of voids analyzed. From this figure, it can be seen that the fracture energy decreases significantly with increasing porosity. The value for zero porosity is strongly influenced by the weakest component, namely the fiber-matrix interfaces (see Table 2). The fracture energy decreases by about 50% (based on mean values) as the porosity increases to 8%, hence it has a strong dependency on defects. The mean values of the fracture energy for the three cases considered are similar and so is the rate of decrease as shown in the solid lines (linear fit). These results indicate that the main parameter affecting the decrease in fracture energy is the porosity, while the size and type of the voids only play a secondary role.
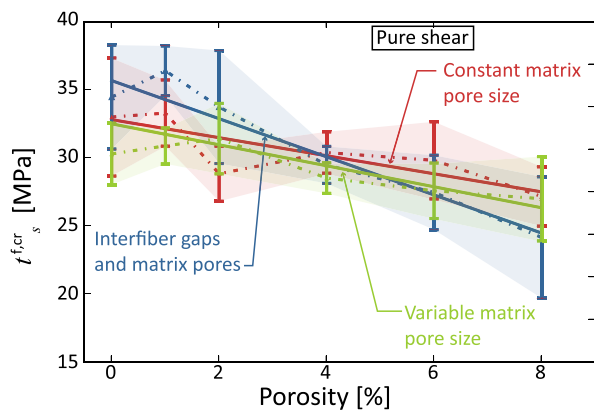
Fig. 11. Tangential component of the effective fracture strength under shear deformation (mode II) as a function of porosity for different types and distributions of defects. The normal component of the effective strength is negligible.

3.5.2. Comparative analysis for pure shear loading (mode II)

For a pure shear deformation, the tangential component $t_s^{f,cr}$ of the effective (macroscopic) fracture strength is shown in Fig. 11 as a function of porosity for the three sets of voids analyzed. The error bars at each porosity analyzed indicate the discrete standard deviation from the mean of the fracture strength. In all simulations, the cracks in the numerical samples open in a nominal mode II. Similar to the mode I case, the fracture strength for the mode II case at zero porosity (no voids) is influenced by the weakest phase (fiber-matrix interface). The strength is about 20% to 30% higher than in mode I for the distinct realizations. The simulations at zero porosity were carried out from distinct sets of microstructures for each void configuration, hence the distinct values reflect the influence of the fiber distribution. From the results in Fig. 11 it can be observed that the mode II strength decreases approximately linearly by about 15% to 30% as the porosity varies from 0% to 8%. The rate of decrease appears slightly larger for the interfiber case, although the difference is marginally significant.

The effective fracture energy G_{II}^c under mode II is shown in Fig. 12 as a function of the porosity for the different types and distributions of voids. Similar to the mode I case, the mode II fracture energy for the zero porosity case is dependent upon the fiber-matrix interface properties (weakest phase). The mean value for zero porosity is about 50% higher than the zero porosity mode I fracture energy. The fracture energy in mode II decreases significantly by about 60% as the porosity increases to 8%, a somewhat larger drop compared to the mode I behavior. Further, the data suggests that the decrease is better approximated with a quadratic function that starts to saturate at the end (i.e., at 8% porosity).
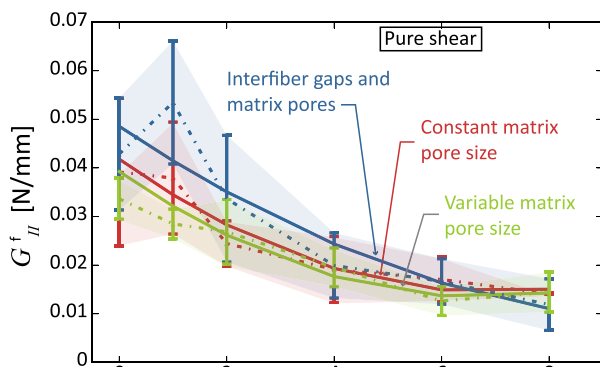

Fig. 12. Effective fracture energy G_{II}^f under shear deformation (mode II) as a function of porosity for different types and distributions of defects.

Observe that the interfiber case appears to have an anomaly at 1% with a slightly higher mean value compared to the no void case, but this difference is not sufficiently significant. It may also be interpreted as a relatively constant mode II fracture strength for small values of the porosity, but the overall trend is that the fracture energy decreases with porosity in all cases. As in the case of mode I, the differences between the types and sizes of voids only appear to play a secondary role while the main significant parameter is the porosity.

Experimental results for transverse fracture strength as a function of porosity with the same set-up as the ones analyzed here do not appear to be readily available in the literature. Nevertheless, it is worth pointing out that experimental measurements for out-of-plane tensile strength of a laminate as well as interlaminar shear strength are qualitatively similar, with reductions of about 50% when the porosity increases from zero to 7% as reported by Bowles and Frimpong (1992); Gurdal et al. (1991); Jeong (1997); Costa et al. (2001). Although comparisons between the aforementioned experiments and the present results should not be done in a one-to-one fashion, the experimental data provides indirect evidence that the order of magnitude of the present simulation results is representative for the actual material system analyzed.

4. Concluding remarks

A new multiscale averaging method has been developed to explicitly study the influence of microvoids in the ply-level behavior of a unidirectional laminate. The method can be readily used for more general composite materials or for micromechanical analysis of fracture in other materials (metals, concrete, etc.). The key ingredient in the method is the separation of the contribution of voids, cracks and bulk and the enforcement of the Hill-mandel condition for a representative surface element (effective crack). The method was applied to study the influence of voids on the transverse fracture strength and fracture energy of fiber-reinfoced unidirectional composites. The main conclusions from the analysis of microvoids in a fiber-reinforced composite are as follows:

- The effective mode I fracture strength remains nearly constant with increasing porosity while there is a large linear decrease in the effective mode I fracture energy.
- There is a significant decrease in both the effective mode II fracture strength (linearly) and energy (quadratically) for increasing porosity
- The porosity is the main parameter influencing the effective fracture properties.
- Microscopic void size and type only play a secondary role in affecting the fracture properties.

The findings in the present study are limited to transverse properties due to computational issues, but the methodology may be extended to coupled three-dimensional cases. Nevertheless, it is expected that simulations involving fiber and matrix cracks may pose computational challenges due to the large differences in fracture properties. Further, other loading cases, in particular compressive loading, may require special treatment due to the unstable fracture mechanisms involved such as kink bands. Nevertheless, these are technologically relevant cases that require attention particularly since defects play a critical role in compressive loading (Kosmann et al., 2015), and the present methodology may be used to study these cases as well.

References

Abaqus, 2018. Finite Element Analysis. www.3ds.com/products-services/simulia/products/abaqus/. Accessed: 2019-1-21.
Arteiro, A., Catalanotti, G., Melro, A.R., Linde, P., Camanho, P.P., 2015. Micro-mechanical analysis of the effect of ply thickness on the transverse compressive strength of polymer composites. Compos. Part A 79, 127–137.

Bosco, E., Kouznetsova, V.G., Geers, M.G.D., 2015. Multi-scale computational homogenization-localization for propagating discontinuities using X-FEM. Int. J. Numer. Methods Eng. 102 (3–4, SI), 496–527.

Bowles, K., Frimpong, S., 1992. Void effects on the interlaminar shear-strength of unidirectional graphite-fiber-reinforced composites. J. Compos. Mater. 26 (10), 1487–1509.

Canal, L.P., Segurado, J., Llorca, J., 2009. Failure surface of epoxy-modified fiber-reinforced composites under transverse tension and out-of-plane shear. Int. J. Solids Struct. 46 (11–12), 2265–2274.

Coenen, E.W.C., Kouznetsova, V.G., Bosco, E., Geers, M.G.D., 2012a. A multi-scale approach to bridge microscale damage and macroscale failure: a nested computational homogenization-localization framework. Int. J. Fract. 178 (1–2, SI), 157–178.

Coenen, E.W.C., Kouznetsova, V.G., Geers, M.G.D., 2012b. Novel boundary conditions for strain localization analyses in microstructural volume elements. Int. J. Numer. Methods Eng. 90 (1), 1–21.

Costa, M.L., de Almeida, S.F.M., Rezende, M.C., 2001. The influence of porosity on the interlaminar shear strength of carbon/epoxy and carbon/bismaleimide fabric laminates. Compos. Sci. Technol. 61 (14), 2101–2108.

Farle, A.-S., Krishnasamy, J., Turteltaub, S., Kwakernaak, C., van der Zwaag, S., Sloof, W.G., 2018. Determination of fracture strength and fracture energy of (metallo-) ceramics by a wedge loading methodology and corresponding cohesive zone-based finite element analysis. Eng. Fract. Mech. 196, 56–70.

Gitman, I., Askes, H., Sluys, L., 2007. Representative volume: existence and size determination. Eng. Fract. Mech. 74 (16), 2518–2534.

Gmsh, 2018. Finite Element Mesh Generator. www.gmsh.info. Accessed: 2019-1-21.

Gurdal, Z., Tomasino, A., Biggers, S., 1991. Effects of processing induced defects on laminate response - interlaminar tensile-strength. SAMPE J. 27 (4), 39–49.

Hamidi, Y.K., Aktas, L., Altan, M.C., 2004. Formation of microscopic voids in resin transfer molded composites. J. Eng. Mater. Technol. 126 (4), 420–426.

Hettich, T., Hund, A., Ramm, E., 2008. Modeling of failure in composites by X-FEM and level sets within a multiscale framework. Comput. Methods Appl. Mech. Eng. Enriched Simulation Methods and Related Topics 197 (5), 414–424.

Hille, T.S., Turteltaub, S., Suiker, A.S.J., 2011. Oxide growth and damage evolution in thermal barrier coatings. Eng. Fract. Mech. 78 (10), 2139–2152.

Jeong, H., 1997. Effects of voids on the mechanical strength and ultrasonic attenuation of laminated composites. J. Compos. Mater. 31 (3), 276–292.

de Jong, G., 2018. Multiscale Modeling of the Effect of Sub-Ply Voids on the Failure of Composites: A progressive Failure Model. Delft University of Technology, Delft Msc thesis.

Kanit, T., Forest, S., Galliet, I., Mounoury, V., Jeulin, D., 2003. Determination of the size of the representative volume element for random composites: statistical and numerical approach. Int. J. Solids Struct. 40 (13–14), 3647–3679.

Kosmann, N., Karsten, J., Schuett, M., Schulte, K., Fiedler, B., 2015. Determining the effect of voids in GFRP on the damage behaviour under compression loading using acoustic emission. Compos. Part B 70, 184–188.

Maragoni, L., Carraro, P., Peron, M., Quaresimin, M., 2017. Fatigue behaviour of glass/epoxy laminates in the presence of voids. Int. J. Fatigue 95, 18–28.

Maragoni, L., Carraro, P., Quaresimin, M., 2016. Effect of voids on the crack formation in a [45/45/0]s laminate under cyclic axial tension. Compos. Part A 91, 493–500. CompTest 2015

Nguyen, V.P., Lloberas-Valls, O., Stroeven, M., Sluys, L.J., 2010. On the existence of representative volumes for softening quasi-brittle materials - a failure zone averaging scheme. Comput. Methods Appl. Mech. Eng. 199 (45–48), 3028–3038.

Park, K., Paulino, G.H., 2011. Cohesive zone models: a critical review of traction-separation relationships across fracture surfaces. Appl. Mech. Rev. 64 (6).

Saeb, S., Steinmann, P., Javili, A., 2016. Aspects of computational homogenization at finite deformations: a Unifying review from Reuss' to Voigt's bound. Appl. Mech. Rev. 68 (5).

Scott, A., Sinclair, I., Spearing, S., Mavrogordato, M., Hepples, W., 2014. Influence of voids on damage mechanisms in carbon/epoxy composites determined via high resolution computed tomography. Compos. Sci. Technol. 90, 147–153.

Suiker, A.S.J., Turteltaub, S., 2007a. Crystalline damage growth during martensitic phase transformations. Philos. Mag. 87 (32), 5033–5063.

Suiker, A.S.J., Turteltaub, S., 2007b. Numerical modelling of transformation-induced damage and plasticity in metals. Modell. Simul. Mater. Sci. Eng. 15 (1, SI), S147–S166. IUTAM Symposium on Plasticity at the Micron Scale, Tech Univ Denmark, Lyngby, DENMARK, MAY 21–25, 2006

Summerscales, J., 1998. Microstructural Characterisation of Fibre-Reinforced Composites. Woodhead Publishing Limited, Cambridge, England.

Svenning, E., Fagerström, M., Larsson, F., 2016a. Computational homogenization of microfractured continua using weakly periodic boundary conditions. Comput. Methods Appl. Mech. Eng. 299, 1–21.

Svenning, E., Fagerstrom, M., Larsson, F., 2016b. On computational homogenization of microscale crack propagation. Int. J. Numer. Methods Eng. 108 (1), 76–90.

Turteltaub, S., van Hoorn, N., Westbroek, W., Hirsch, C., 2018. Multiscale analysis of mixed-mode fracture and effective traction-separation relations for composite materials. J. Mech. Phys. Solids 117, 88–109.

Unger, J.F., 2013. An FE2-X1 approach for multiscale localization phenomena. J. Mech. Phys. Solids 61 (4), 928–948.

Vajari, D.A., 2015. A micromechanical study of porous composites under longitudinal shear and transverse normal loading. Compos. Struct. 125, 266–276.

Vajari, D.A., Gonzalez, C., Llorca, J., Legarth, B.N., 2014. A numerical study of the influence of microvoids in the transverse mechanical response of unidirectional composites. Compos. Sci. Technol. 97, 46–54.

Vajari, D.A., Legarth, B.N., Niordson, C.F., 2013. Micromechanical modeling of unidirectional composites with uneven interfacial strengths. Eur. J. Mech. A 42, 241–250.

Xia, Z., Curtin, W., Peters, P., 2001. Multiscale modeling of failure in metal matrix composites. Acta Mater. 49 (2), 273–287.